ADVANCED INTELLIGENT SYSTEMS
Open Access
www.advintellsyst.com

Modeling and Experimental Validation of High-Flow Fluid-Driven Membrane Valves for Hyperactuated Soft Robots

*Tianxiang Dai, Nikola Velimirović, Philipp Zalles, Daniel Bruder, Keith Buffinton, R. Brent Gillespie, and C. David Remy**

Herein, the design, modeling, and validation of high-flow, fluid-driven, membrane valves tailored specifically for applications in soft robotic systems are described. Targeting the *piping problem* in hyper-actuated soft robots, two fluid-driven membrane valve designs that can admit flows of up to 871 mg s^{-1} while weighing less than 20 g are introduced. A mathematical model to predict fluid flow by representing the displacement of the membrane as a scalar quantity influenced by the balance of pressures applied across the valve's ports is established. The model incorporates six parameters with direct physical relevance, enhancing its usefulness in valve design and system integration. In an experimental validation, flow rates with deviations within 4% are predicted and the onset of flow is correctly identified with an error rate of less than 1%. In addition, applications of these valves for flow amplification and for the creation of a fluid-driven oscillator are experimentally demonstrated. This research contributes to the advancement of soft robotics by providing a tool for designing, optimizing, and controlling fluid-driven systems and it lays the groundwork for the future development of embedded, fluid-controlled valve networks that can be used to realize hyper-actuated soft robotic systems.

1. Introduction

An important class of soft robotic systems includes fluid-driven robots made of elastomeric materials that are equipped with reinforcing structures. Such systems have been used in human–robot collaboration, the navigation of difficult terrain, and the handling of delicate objects.[1–3] Given their monolithic design, they are relatively easy and inexpensive to manufacture and can be completely encapsulated for protection against environmental factors.[4–6] They also have the potential for greater cost-efficiency as complexity increases. In theory, the expense associated with the production of more complex soft robots featuring higher numbers of actuators does not increase nearly as sharply as with hard-bodied robots driven by conventional electric actuators.[7] Since soft robots are made using additive manufacturing or casting, it is less relevant how many actuator cells are embedded in a certain volume of substrate. This cost scaling lends itself to the development of hyper-actuated systems with dozens or potentially thousands of actuator cells which could perform highly complex motions or exhibit targeted spatial deformations.

To enable this level of complexity, we must, however, solve a substantial challenge, the *piping problem*. In most existing soft fluidic robot designs, each individual actuator cell requires a dedicated fluid supply and fluid control system, which in turn limits the number of actuator cells, as this required piping takes up a significant volume.[3,4,8–13] In some systems with many actuated degrees of freedom, the piping actually extends beyond the envelope of the robot itself. That is, the control tubing lies on the outside of the main soft robot arm.[14,15] To control the fluid flow, external electromagnetic valves are used, which require additional mass and volume and which can substantially drive up the cost of the system despite the price benefits in manufacturing.[16] **Figure 1**A showcases the piping problem on a soft robotic arm from our lab. The lower section consists of four FREE actuators, which are individually driven by their respective fluid supply lines. Even with this simple two-stage design, we see the overflowing of tubing outside of the envelope of the robot; this issue would be greatly accentuated when trying to move toward a hyperactuated robotic system.

T. Dai, N. Velimirović, P. Zalles, C. D. Remy
Institute for Nonlinear Mechanics
University of Stuttgart
Stuttgart 70569, Germany
E-mail: david.remy@inm.uni-stuttgart.de

D. Bruder, R. B. Gillespie
Mechanical Engineering
University of Michigan
Ann Arbor, MI 48109, USA

K. Buffinton
Mechanical Engineering
Bucknell University
Lewisburg, PA 17837, USA

R. B. Gillespie
Robotics
University of Michigan
Ann Arbor, MI 48109, USA

The ORCID identification number(s) for the author(s) of this article can be found under https://doi.org/10.1002/aisy.202300864.

DOI: 10.1002/aisy.202300864

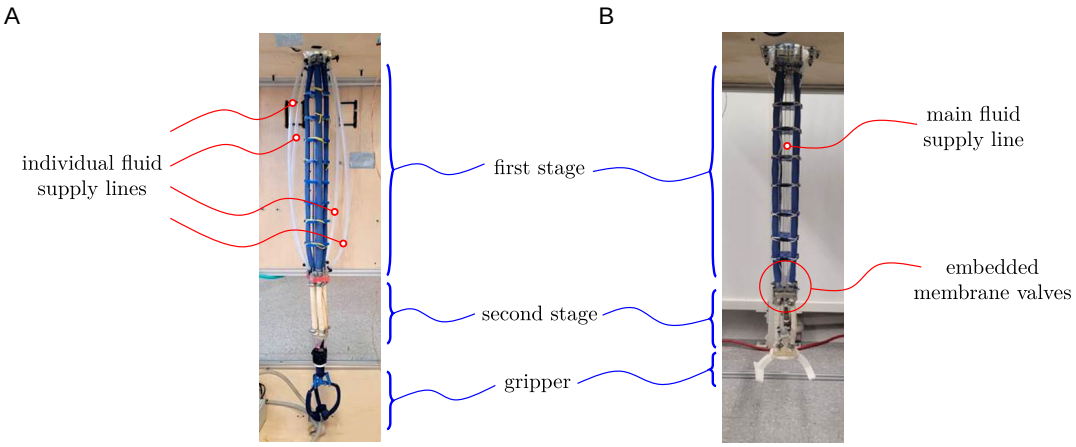

Figure 1. Comparison between two versions of a soft robotic arm: the initial version A) using individual fluid supply lines for the second-stage actuators, with piping extending beyond the envelope of the robot, and the updated version B) using local, embedded valves, with the main fluid supply located inside the robot.

A promising solution to the piping problem lies in the separation of power and signal and the multiplexing of information through a fluid logic system. By adopting local, embedded valves, we could use a single main fluid supply for power, eliminating the need for each actuator to have its own dedicated fluid supply. In contrast to individual connections, this main power line only needs to be sized to supply the maximum power required by all actuators expected to be active at one time. This value is often much smaller than the sum of the individual maximal powers of the actuators, which would dictate the size of the individual fluid supplies. Enabling such a decentralized valve design requires the valves to be small and lightweight, which can be achieved with *high-flow* fluid-driven valves, which are economical to manufacture and allow for a lightweight and compact design compared to their equivalent electromagnetic counterparts.[17] It can be shown that, if the control lines for these valves are of a reasonably small cross section, transitioning to a system with one primary fluid supply line and numerous thin control lines can significantly reduce the overall piping footprint. To achieve this, the valves should have sufficiently high flow rate capabilities to enable high-bandwidth actuation of the actuators. Figure 1B depicts the updated version of our soft robotic arm and showcases the benefits of integrating local embedded valves into the robot's structure. A single main fluid supply line feeds the bottom four FREE actuators, with four small-diameter signal lines used for the control of the valves. We observe a net decrease of 19% in tubing cross-sectional area, and all tubing is now integrated inside of the robot.

To further minimize the number of control lines, we can draw from the field of microfluidics, where networks of elastomeric valves have been used to multiplex information sent through a smaller number of control lines. To replace a parallel configuration of control lines, information is encoded in time or using binary and other encoding schemes within a significantly smaller set of control lines. This approach to the piping problem has been termed *fluid logic* within the microfluidics or lab-on-a-chip industry.[5,18] For example, a binary encoded three-bit addressing stage with a single "data" line requires only four fluid lines, but can drive eight actuator cells.[19] The components necessary for such a fluid-logic circuit can also be based on the use of fluid-driven valves and can be manufactured very much the same way as their high-flow counterparts.

Previous studies on fluid-driven valves have made significant contributions to the field, primarily focusing on aspects of fluid logic and pressure modeling. For instance, Jensen et al.[20] showcased pneumatic digital logic gates using fluid-driven valves as transistors. Russomanno et al.[21] delved into the concept of pressure gain, providing new insights into the cascadability of fluid logic elements, thus enabling large-scale fluidic circuits. Rothemund et al.[22,23] employed kinking tubes to create a bistable soft valve, acting as a fluidic switch and enabling fluidic oscillators given a constant pressure source. Finally, Hoang et al.[19] described how signals can be digitally multiplexed through the use of fluid-driven logic gates.

In the realm of valve fabrication, significant strides have been made in both vacuum-based and pressure-based systems. Grover et al.[24] laid the groundwork for monolithic membrane valves, sandwiching a membrane between glass etched with fluidic channels. These are mirror symmetric by design, that is, the inflow and outflow chambers are separated by a straight barrier. Rhee and Burns[18] explored the use of polydimethylsiloxan (PDMS) for building pneumatic logic circuits, and Duncan et al.[25] focused on the scaling of these circuits, using precision machining techniques to reduce the size of the valves. On the pressure-based front, Weaver et al.[26] presented a pneumatic valve constructed utilizing soft-lithography processes. Finally, Devaraju et al.[17] concentrated on the creation of normally closed pressure-based valves, using a flash curable material to create an artificial seat height of the valve.

These works lay the foundation for how valves respond to various fluidic inputs and enable the construction and modeling of fluidic gates and circuits. Inherently, the valves used for logic circuits do not have the need and capacity for high flow rates, as the volumes present in the circuit are relatively small. As such, the valves developed in previous work are impractical for driving pneumatic actuators with larger volumes.

In order to enable cost-effective hyperactuated soft robotic systems, which are driven by distributed and fluid-controlled valve networks that are directly embedded in the robots' structure, we need to scale up fluid-driven membrane valves from the domain of microfluidics as well as to develop a better understanding of their physical properties and dynamics. This involves not just a detailed exploration of the opening and closing mechanics of the valve, but also a comprehensive assessment of the mass flow passing through the valve under various control signal values. The two key properties in this context are the amplification of pressure for the logic stage of the system (the so-called *pressure gain*) and the flow capabilities of the valve for the amplification stage. A physics-based mathematical model of these properties will be an invaluable tool in the design and control of such hyperactuated, fluid-driven soft robotic systems.

In this article, we present the design of two high-flow valves (Section 2) and develop a mathematical model that provides a detailed physics-based understanding of the valve dynamics (Section 3). The valves are based on a sandwiched membrane design and manufactured on a 3D printer. The model, at its core, is based on an estimation of the displacement of the membrane. This displacement is assumed to be a direct result of the pressure difference across the two sides of the membrane and the displacement in turn creates a variable resistance across the flow channel. Using a quadratic flow law, this resistance finally leads to an estimation of the flow rate. The model formulation is parameterized with a total of six variables which are carefully chosen to represent physically relevant properties of the valve, thus providing a scientific basis for the design and control of such fluid-driven valve systems. In Section 4, we detail the methods used for parameter identification and introduce the experimental setup to validate the model. The results of these experiments, which investigate not only the overall prediction accuracy, but also the individual assumptions that went into the modeling framework, are presented in Section 5. To showcase the real-world applicability of our membrane valves with the corresponding mathematical model, we demonstrate the valves flow amplification and fluid logic properties in two experiments in Section 6. We conclude with a discussion of these contributions in Section 7.

2. Design

This article presents a model and experimental evaluation of small-scale, fluid-driven membrane valves. These valves operate through the use of fluid pressure imposed in a *control chamber* which pushes a membrane against the valve seat, creating a seal that stops the flow of fluid from the *inflow chamber* to the *outflow chamber*. When the fluid pressure p_{ctrl} in the control chamber is reduced, the membrane is pushed out of the way by the pressures p_{in} and p_{out}, allowing fluid to flow from the inflow to the outflow chamber due to the pressure difference (**Figure 2**). To create a pressure offset, the valve design may feature a seat raised by a height h_{seat}, which pre-tensions the membrane and reduces the value of p_{ctrl} needed to close the valve.

We investigate two types of valves that differ primarily in the geometry of their inflow and outflow chambers. The first valve is *axi-symmetric*, where a round inflow chamber (with diameter d_{in}) is separated by an annular wall (with width w_{seat}) from the surrounding outflow chamber (with diameter d_{out}). The different shapes of the inflow and outflow chambers introduce a flow direction dependency, and the axi-symmetric valves can thus only be used with the input pressure being applied to the central chamber. Using the valves in reverse results in substantial leakage from input to output. For this reason, we also designed a second valve with *mirror-symmetry*, to specifically study the dependency on the direction of flow. In our version, the inflow and outflow chambers are semicircular in shape (with diameter d_{io}) and are separated by a straight valve seat with width w_{seat}.

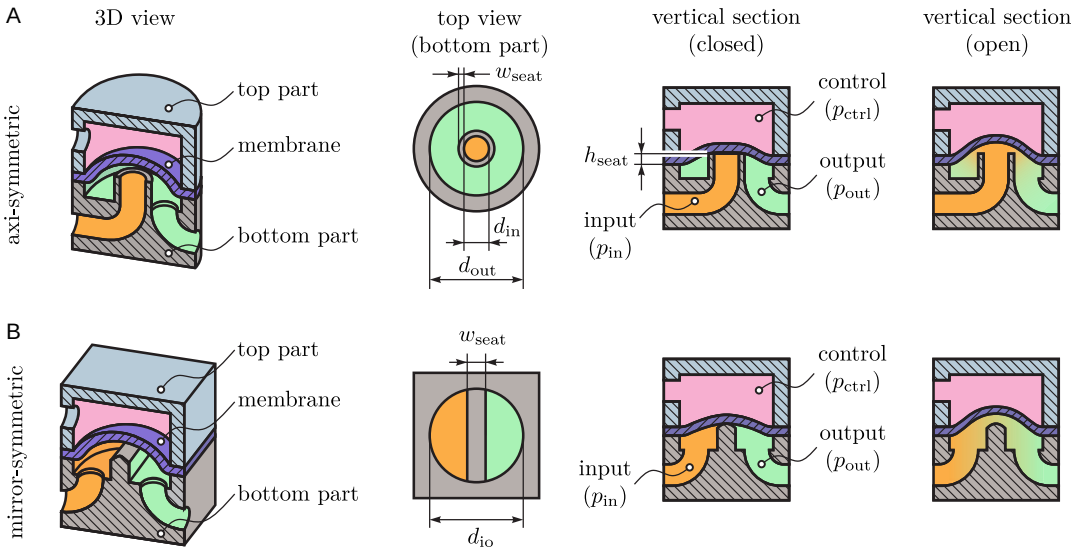

Figure 2. Schematic illustration of the *axi-symmetric* (A, top row) and *mirror-symmetric* (B, bottom row) valves used in this study. Shown are, from left to right: a three dimensional view of each valve sectioned by a vertical plane; a top view of the bottom part of each valve showing inflow and outflow chambers; a vertical cross section of each valve in its closed; and open state.

As both chambers are identical, we expect this valve to behave similarly when operated in either flow direction.

The mirror-symmetric valves are the common choice in microfluidics,[19–21] as they are easy to manufacture using soft lithography techniques.[27] They can admit flow in both directions, but are limited in the choice of the seat height. To ensure a tight seal between the membrane and the valve seat, the seat would need to be curved up from the edges toward the center. The axi-symmetric valves, in contrast, can only be manufactured using 3D printing and can only be used in unidirectional flow. Their big advantage is the large variability in possible seat height, which we were able to turn to precise dimensions on a lathe. The axi-symmetric valve seat and round membrane create an even seal for a wide range of seat heights h_{seat}.

Both valve types consist of two 3D printed parts, a top part that houses the control chamber and a bottom part that houses the inflow and outflow chambers. These parts were printed on a Sinterit *Lisa Pro* SLS-Printer from polypropylene material, using a layer height 0.125 mm. To increase precision, the connecting surfaces and the valve seat of the axi-symmetric valves were post-processed on a lathe. The mirror-symmetric valves did not undergo any postprocessing. A membrane made from 0.5 mm *Vulkollan* polyurethane was mounted between these two parts to separate the control chamber from the inflow and outflow chambers. Prior to assembly, the membrane was slightly pretensioned in an embroidery hoop to avoid any wrinkles or folds. Pressure-sensitive adhesive tape (3M transfer tape 950, 0.13 mm) was used to connect the components and to ensure an airtight seal. In addition, screws were used to assemble the sandwich structure, ensuring that it would withstand internal pressure without leakage. The holes needed for these screws were punched into the membrane only after the initial assembly was completed, in order to maintain an even pretension of the membrane. To complete the valve, small segments of pneumatic hose were affixed with adhesive into the holes that connect the three chambers, forming the input, output, and control ports of the valve. Photographs of both valves, with their respective computer-aided design (CAD) renderings, are shown in **Figure 3**.

3. Modeling

To describe the behavior of fluid-driven valves such as the ones presented in Section 2, we present a physics-based and empirically supported model that predicts the mass flow rate $\dot{m}$ of a compressible fluid as a function of the pressures p_{in}, p_{out}, and p_{ctrl} at the input, output, and control ports of the valve. Without loss of generality, we limit ourselves to a unidirectional flow through the valve, that is, we assume $p_{\text{in}} > p_{\text{out}}$ and $\dot{m} \geq 0$. We characterize the deformation of the membrane inside the valve by a single scalar displacement variable d and determine this displacement from a balance of pressures and elastic forces across the membrane. This balance is based on three effective cross-sectional areas that are associated with each of the three pressures. Notably, these effective areas differ from the geometrical cross-sectional areas of the physical chambers that are connected to the three ports. Due to the fluid flow, the effective area associated with the input pressure is typically larger than the corresponding geometrical area, while the effective area associated with the output pressure is smaller than its geometrical area (see **Figure 4**). Empirically, we found that the size of these effective areas was not influenced by the magnitude of flow and thus represent them as flow-invariant parameters. We will revisit this assumption in Section 5.3. In the model, we further assume that the fluidic resistance R of the flow channel depends nonlinearly

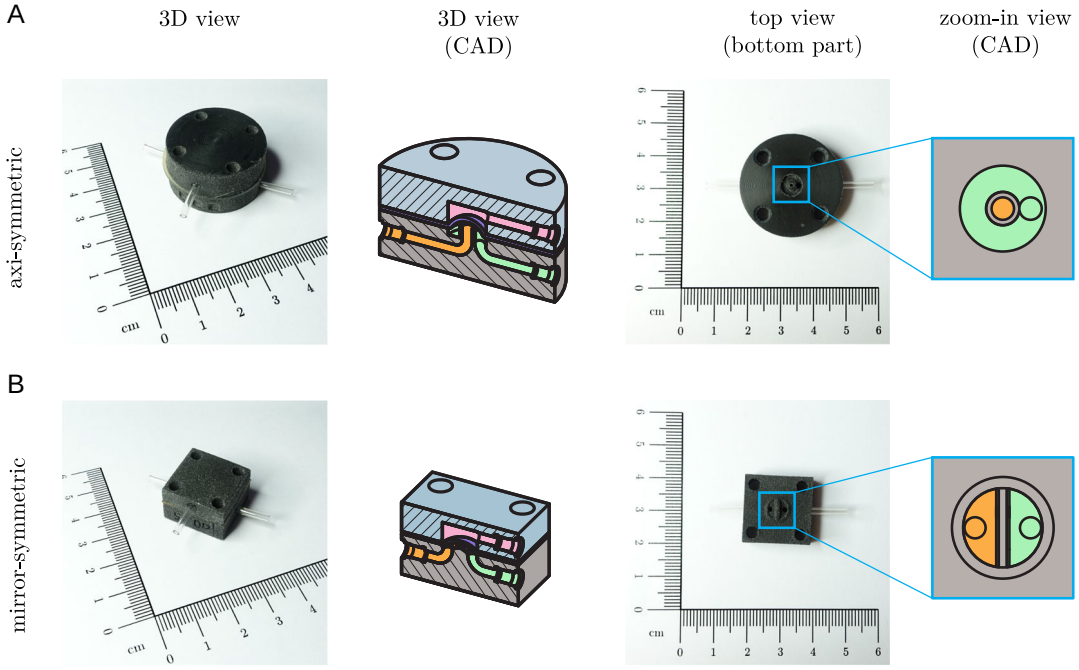

Figure 3. Visual comparison of A) the *axi-symmetric*, top row, and B) *mirror-symmetric*, bottom row valves against their corresponding CAD renderings. For improved visualization, the top part is rotated 90 degrees in the 3D sectional view within the CAD environment.

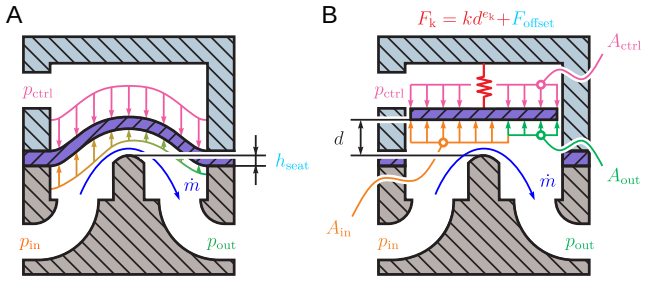

Figure 4. The action of the membrane in the valve (shown in A) is modeled as a piston connected to a stiffening spring (shown in B). The effective areas A_{in} and A_{out}, over which the pressures p_{in} and p_{out} act, are a simplified description of a continuous pressure distribution along the flow path of the fluid. The piston's displacement d is then used to scale the resistance of the flow path. As d is measured from the top of the valve seat and not from the height of the undeformed membrane, an offset force F_{offset} is introduced which models the pretension of the membrane by the seat height h_{seat} (both shown in sky blue). While this schematic only shows the mirror-symmetric valve, the same model is used for the axi-symmetric version.

on the displacement variable d. Together with the input and output pressures p_{in} and p_{out}, we use this resistance to predict the mass flow rate through the valve. We present the three components of this model in the following sections.

3.1. Resistance of a Fluidic Channel

The pressure drop δp of an isothermal flow across a restriction in a channel is given by $\delta p = \zeta \rho \frac{1}{2} \bar{v}^2$, with loss coefficient ζ, fluid density ρ, and average velocity $\bar{v}$ (Equation (6)–(8)) in ref. [28]). When modeling a pneumatic valve, we must account for the fact that air as a compressible fluid has varying pressure and density and that it will encounter varying geometries throughout the channel. As a consequence, we apply this equation for an infinitesimally short section dx of the channel. This section dx is associated with an infinitesimal loss $d\zeta = \bar{\zeta} dx$ (where $\bar{\zeta}$ is the loss per distance), which causes an infinitesimal pressure drop of $-dp$. Note that the minus sign follows from the definition of pressure drop as $\delta p = p_{in} - p_{out}$. Substituting the fluid velocity with $\bar{v} = \frac{\dot{m}}{\rho A}$ and using the ideal gas law to write the density as $\rho = \frac{M}{R_{gas} T} p$, this yields

$$-2p(x)dp = \frac{R_{gas} T}{M} \dot{m}^2 \frac{\bar{\zeta}(x)}{(A(x))^2} dx \tag{1}$$

Here, the mass flow rate $\dot{m}$, molar mass M, universal gas constant R_{gas}, and absolute gas temperature T are constant along the flow path, while the cross section $A(x)$, the loss-per-distance $\bar{\zeta}(x)$, and the pressure $p(x)$ vary along the channel. Integrating both sides of Equation (1) over the length L of the channel yields

$$\int_{p_{in}}^{p_{out}} -2p(x)dp = -p_{out}^2 + p_{in}^2 = \dot{m}^2 R^2 \tag{2}$$

where p_{in} and p_{out} are the pressures at the input and output of the channel, respectively, and where we have defined

$$R := \sqrt{\frac{R_{gas} T}{M} \int_0^L \frac{\bar{\zeta}(x)}{(A(x))^2} dx} \tag{3}$$

to characterize the resistance of the channel to a specific fluid. With this resistance and under the above assumptions, the mass flow rate $\dot{m}$ through a channel is proportional to the square root of the difference in squares of the input and output pressures p_{in} and p_{out}:

$$\dot{m} = \frac{1}{R} \sqrt{p_{in}^2 - p_{out}^2} \tag{4}$$

In addition to computing $\dot{m}$, the structure in Equation (4) allows us to reason about the flow through two (or more) resistors connected in series. Let us denote the pressure at the input of a first resistor (with a resistance value R_{12}) as p_1 and the pressure at its output as p_2. If another resistor is connected in series, the pressure p_2 is simultaneously the input pressure of the second resistor, while the mass flow rate $\dot{m}$ through both resistors has to be the same. Suppose this second resistor (with a resistance value R_{23}) has an output pressure of p_3. Due to Equation (4), it must hold that $p_1^2 - p_2^2 = R_{12}^2 \dot{m}^2$, and $p_2^2 - p_3^2 = R_{23}^2 \dot{m}^2$. We can sum up these two relationships to yield $p_1^2 - p_3^2 = (R_{12}^2 + R_{23}^2)\dot{m}^2 = R_{13}^2 \dot{m}^2$, where R_{13} describes the combined resistance between the input of the first resistor and the output of the second. That is, when two resistances are connected in series, their values are added in quadrature:

$$R_{13} = \sqrt{R_{12}^2 + R_{23}^2} \tag{5}$$

In a membrane valve, the resistance R is variable and depends on the displacement of the membrane caused by the three pressures applied to the valve. Given the complex geometry, we cannot rely on the integral in Equation (2) to determine R. Instead, in our model, we assume that scales as a function of the variable d that we use to characterize the displacement of the membrane. We will identify the parameters of this scaling law experimentally. To understand its structure, we take insights from simpler geometries. For channels with a constant cross section A and a constant loss-per-distance $\bar{\zeta}$, the resistance R can be computed by solving the integral in Equation (3) analytically. For cylindrical pipes, for example, the resistance is given by the Weymouth equation (Equation (9)–(17)) in ref. [29]):

$$R := 8 \sqrt{\frac{f L R_{gas} T}{\pi^2 D^5 M}} \tag{6}$$

where the resistance depends on the specific geometry of the pipe, expressed in the diameter D, pipe length L, and friction factor f (note that Equation (5)–(8) in ref. [28] uses the Darcy friction factor λ, which is equal to $4f$). Here the loss-per-distance is given as $\bar{\zeta} = \frac{4f}{D}$ and the cross section as $A = \frac{\pi D^2}{4}$. Extensions of this equation exist for noncylindrical conduits, in which D is replaced by an equivalent *hydraulic diameter*.[29] Equation (6) can provide a useful guideline for understanding the qualitative scaling effects we can expect. Assuming an isothermal flow in a nearly constant Reynolds regime, the friction factor f and the temperature T can be considered to be constant values.

The equation further involves geometry-dependent variables such as L in the numerator and D^5 in the denominator. That is, the geometric parameters enter the equation multiplicatively and with different exponents. This indicates that the resistance of a valve in which the geometry varies with the displacement variable d will likely be proportional to d^{-e_r}, where e_r is an exponent we will determine experimentally. We chose a negative sign in the exponent, as the variable D that describes the cross section in Equation (6) dominates the equation with a negative exponent.

3.2. Force Balance across the Membrane

To account for the balance of pressures and elastic forces across the membrane, we make two important simplifying assumptions. First, we characterize the deformation of the membrane by a single scalar displacement d. We model the elastic forces F_k that are created by this displacement as a stiffening spring to capture the stiffening properties of a deflecting membrane. This leads to a nonlinear elastic force law of the form

$$F_k = kd^{e_k} + F_{\text{offset}} \tag{7}$$

with stiffness k and an exponent $e_k > 0$. The force F_{offset} is the representation of the pretension of the membrane that is induced by the seat height h_{seat} of the valve, which puts load on the piston for no displacement, that is, $d = 0$.

As a second modeling assumption, we approximate the continuous distribution of pressures on the flow-channel side of the membrane as a discrete distribution characterized by areas A_{in} and A_{out} over which p_{in} and p_{out} act. This allows us to assign each pressure in the system to a fixed effective cross-sectional area. In our model, we further assume that these areas remain constant regardless of the flow's magnitude or the membrane's displacement d. We will revisit this assumption in Section 5.3. With this, we can compute the force ΔF_{p} that is created by the pressure difference between the two sides of the membrane as:

$$\Delta F_{\text{p}} = A_{\text{in}}p_{\text{in}} + A_{\text{out}}p_{\text{out}} - A_{\text{ctrl}}p_{\text{ctrl}} \tag{8}$$

Here, p_{in}, p_{out}, and p_{ctrl} are the pressures on the input, output, and control ports of the valve and the values A_{in}, A_{out}, and A_{ctrl} are the equivalent cross-sectional areas across the membrane that are associated with these pressures.

To help clarify the modeling assumptions made above, we can draw an analogy with a model that replaces the membrane with a friction-free piston. This piston is connected to a nonlinear spring that describes the restoring force of the elastic membrance and has two distinct areas over which the pressures p_{in} and p_{out} act. This model is visualized in Figure 4.

In a state of static equilibrium, the pressure-generated force ΔF_{p} and the elastic force F_k are in balance, that is, $\Delta F_{\text{p}} = F_k$. To calculate the equilibrium position of the membrane, we must also take into account that the displacement d of the membrane is constrained to positive values only, because the motion of the membrane is limited in the opposite direction by the valve seat. This yields

$$d = \begin{cases} 0 & , \quad \Delta F_{\text{p}} \le F_{\text{offset}} \\ \left(\dfrac{\Delta F_{\text{p}} - F_{\text{offset}}}{k}\right)^{\frac{1}{e_k}} & , \quad \Delta F_{\text{p}} > F_{\text{offset}} \end{cases} \tag{9}$$

3.3. The Valve as a Variable Resistance

According to Equation (5), the total resistance of the valve R can be modeled as $R = \sqrt{R_{\text{f}}^2 + R_{\text{v}}^2}$, where R_{f} models the fixed resistance that is inherent to the conduits connected to the input and output ports and that acts in series with the variable resistance R_{v} across the valve itself. As stated above, we model the variable resistance R_{v} to be proportional to d^{-e_r}. The exponent $-e_{\text{r}}$ is negative ($e_{\text{r}} > 0$), as the resistance of the valve is dominated by the cross section of the channel, which appears in the denominator of Equation (6). For $\Delta F_{\text{p}} > F_{\text{offset}}$, we thus obtain

$$R_{\text{v}} = rd^{-e_r} = r\left(\frac{\Delta F_{\text{p}} - F_{\text{offset}}}{k}\right)^{-\frac{e_r}{e_k}} \tag{10}$$

with r being a constant of proportionality. For ΔF_{p} approaching F_{offset}, the displacement d will be zero and R_{v} will tend toward infinity. That is, the flow will be completely blocked. Using the total resistance in Equation (4) yields

$$\dot{m} = \begin{cases} 0 & , \quad \Delta F_{\text{p}} \le F_{\text{offset}} \\ \dfrac{\sqrt{p_{\text{in}}^2 - p_{\text{out}}^2}}{\sqrt{R_{\text{f}}^2 + R_{\text{v}}^2}} & , \quad \Delta F_{\text{p}} > F_{\text{offset}} \end{cases} \tag{11}$$

3.4. Suitable Parameter Choices

The model of the resistance in Equation (10) comes with a number of parameters that need to be identified from data. In the given formulation, these parameters are not independent. For example, we can reduce the fraction $\frac{e_r}{e_k}$ to a single parameter. Similarly, we can simplify the product of r, k^{-1}, and the areas in ΔF_{p}. That is, through appropriate substitutions, we can reduce the number of parameters from 9 to 6 and convert Equation (10) into a simpler format, which also better reveals the physical significance of the experimentally determined parameters. With such substitutions, we rewrite R_{v} as

$$R_{\text{v}} = R_{\text{f}}\left(\frac{\Delta p - p_{\text{close}}}{p_{\text{trans}} - p_{\text{close}}}\right)^{-e} \tag{12}$$

where Δp is obtained by normalizing ΔF_{p} by A_{ctrl} to yield an *equivalent pressure difference* across the membrane:

$$\Delta p = \frac{\Delta F_{\text{p}}}{A_{\text{ctrl}}} = a_{\text{in}}p_{\text{in}} + a_{\text{out}}p_{\text{out}} - p_{\text{ctrl}} \tag{13}$$

Each of the parameters in Equation (12) describes a distinct property of the valve.

The *fixed resistance*

$$R_{\text{f}} \coloneqq R_{\text{f}} \tag{14}$$

characterizes the size of the valve. More precisely, it determines the amount of flow the valve can admit when it is fully open.

The *closing pressure*

$$p_{\text{close}} := \frac{F_{\text{offset}}}{A_{\text{ctrl}}} \tag{15}$$

determines the value of the equivalent pressure difference Δp at which the term under the exponent in Equation (12) becomes 0 and the variable resistance R_{v} thus becomes infinite. For $\Delta p \leq p_{\text{close}}$, the valve will fully close. The parameter p_{close} is closely related to the *pressure gain* in fluid logic circuits.[21] Larger values of p_{close} mean that less control pressure p_{ctrl} is necessary to close the valve. Since p_{close} is the pressure equivalent of the offset force that results from the pretension of the membrane, it will be influenced by the height of the valve seat.

The *relative effective areas*

$$\begin{aligned} a_{\text{in}} &:= \frac{A_{\text{in}}}{A_{\text{ctrl}}} \\ a_{\text{out}} &:= \frac{A_{\text{out}}}{A_{\text{ctrl}}} \end{aligned} \tag{16}$$

describe the relative contribution of the input and output pressures to the force balance across the membrane. They determine the sensitivity of the valve with respect to these pressure values and should sum up to one to make the total area on both sides of the membrane equal.

The *transition pressure*

$$p_{\text{trans}} := \frac{k}{A_{\text{ctrl}}} \left(\frac{r}{R_{\text{f}}} \right)^{\frac{e_k}{e_{\text{r}}}} + p_{\text{close}} \tag{17}$$

characterizes the value of the equivalent pressure difference Δp at which the term under the exponent in Equation (12) becomes 1 and the variable resistance R_{v} is thus equal to the fixed resistance R_{f}. That is, for $\Delta p > p_{\text{trans}}$ the fixed resistance R_{f} starts to dominate the flow. At this transition point, the total resistance R is equal to $\sqrt{2}R_{\text{f}}$. Conversely, the conductivity (inverse resistance) reaches $\frac{1}{\sqrt{2}R_{\text{f}}}$ and thus 71% of its maximal value of $\frac{1}{R_{\text{f}}}$ which is reached when the valve is fully open.

Finally, the *exponent*

$$e := \frac{e_{\text{r}}}{e_k} \tag{18}$$

describes the linearity of the opening characteristic. An exponent $e = 1$ would be a linear opening characteristic, whereas for $e > 1$ the valve would initially open slowly and then more rapidly in response to changes in p_{ctrl}. To get a rough estimate for the value of e, we can make the approximation $D \approx d$, neglect all other geometric effects in the flow channel, and assume a nearly linear spring with $e_k \approx 1$. According to Equation (6), this would lead to $R_{\text{v}} \propto d^{-e_{\text{r}}} \approx d^{-2.5} \approx \Delta p^{-2.5}$. Consequently, we would expect the exponent e to have a nominal value of $e \approx 2.5$.

With these substitutions, the flow predicted by Equation (11) becomes

$$\dot{m} = \begin{cases} 0 & , \quad \Delta p \leq p_{\text{close}} \\ \dfrac{\sqrt{p_{\text{in}}^2 - p_{\text{out}}^2}}{R_{\text{f}} \sqrt{1 + \left(\frac{\Delta p - p_{\text{close}}}{p_{\text{trans}} - p_{\text{close}}} \right)^{-2e}}}, & \Delta p > p_{\text{close}} \end{cases} \tag{19}$$

4. Experimental Section

4.1. Parameter Fitting

The six parameters were determined experimentally. Yet, rather than fitting them directly to raw input–output data, we performed the parameter identification in two separate stages.

First, we characterized the opening/closing characteristic of the valve. That is, we focused on the condition $\Delta p = p_{\text{close}}$. With the definitions of Equation (12), this condition leads to the implicit equation $a_{\text{in}} p_{\text{in}} + a_{\text{out}} p_{\text{out}} - p_{\text{ctrl}} - p_{\text{close}} = 0$, which describes a hyperplane in the 3D space of pressure values. More specifically, this hyperplane separates the data points that correspond to an open valve from those that correspond to a closed valve. After labeling the data points accordingly, we identified this separating hyperplane by training a soft margin linear support vector machine. To this end, we defined $\mathbf{x}_i = \begin{bmatrix} p_{\text{in},i}, & p_{\text{out},i}, & p_{\text{ctrl},i} \end{bmatrix}^T$ as the input vector of each data point. The data point was classified as *valve open* ($\text{y}_i = +1$) if the flow was above a threshold of $\dot{m}_{\text{min}}$, and *valve closed* ($\text{y}_i = -1$) below $\dot{m}_{\text{min}}$:

$$\begin{aligned} \mathbf{x}_i &= \begin{bmatrix} p_{\text{in,i}}, & p_{\text{out,i}}, & p_{\text{ctrl,i}} \end{bmatrix}^T \\ \text{y}_i &= \begin{cases} +1, & \dot{m}_i > \dot{m}_{\text{min}} \\ -1, & \dot{m}_i \leq \dot{m}_{\text{min}} \end{cases} \end{aligned} \tag{20}$$

With this, we solved the quadratic program

$$\begin{aligned} \min_{\mathbf{w}, b, \xi_i} \quad & \frac{1}{2} \mathbf{w}^T \mathbf{w} + C \sum_{i=1}^{n} \xi_i \\ s.t. \quad & \text{y}_i (\mathbf{w}^T \mathbf{x}_i + b) + \xi_i \geq 1 \\ & \xi_i \geq 0 \end{aligned} \tag{21}$$

where C constitutes a weighting factor on the slack variables ξ_i, and the constraints are given individually for each data point $1 \leq i \leq n$. The model parameters can then be taken from the normal vector $\mathbf{w} = [w_{\text{in}}, w_{\text{out}}, w_{\text{ctrl}}]^T$ and the intercept b of the hyperplane as

$$\begin{aligned} a_{\text{in}} &= -w_{\text{in}} / w_{\text{ctrl}} \\ a_{\text{out}} &= -w_{\text{out}} / w_{\text{ctrl}} \\ p_{\text{close}} &= b / w_{\text{ctrl}} \end{aligned} \tag{22}$$

In a second step, we identified the fixed resistance R_f, the transition pressure p_{trans}, and the exponent e . To this end, we performed a nonlinear least-squares fit on all data with an open valve, that is, with $\Delta p_i > p_{\text{close}}$. Here, we fit the data to $\frac{1}{R}$ rather than R, to avoid issues created by the infinite resistance values of the closed valve. Input data x_{i} were the equivalent pressure differences $x_{\text{i}} = \Delta p_i$, and output data y_{i} were the inverse resistance values $\frac{1}{R}$ computed from the measured data:

$$y_i = \frac{1}{R_i} = \frac{\dot{m}_i}{\sqrt{p_{\text{in},i}^2 - p_{\text{out},i}^2}} \tag{23}$$

This data was fit on the function

$$y = \frac{1}{R_f \sqrt{1 + \left(\frac{x - p_{\text{close}}}{p_{\text{trans}} - p_{\text{close}}}\right)^{-2e}}} \tag{24}$$

with R_f, p_{trans}, and e being the free parameters.

4.2. Experimental Setup

The pressure regulators and sensors used in this experimental setup were intrinsically designed to use gauge pressure. This is in contrast to the model presented in this article which, due to its quadratic terms, requires absolute pressure values as input. In order to use a consistent expression of pressure, in the following, we converted the setpoint values and actual measurements in gauge pressure into absolute pressure for use in the analysis using a barometric offset of 96 kPa corresponding to an altitude of 480 m.[30] In our experimental setup, the desired pressures on the input and output port were regulated by Festo VPPM pressure regulators (106–1096 kPa pressure range, 12.5 kPa accuracy) and the pressure on the control input by a Festo VEAB pressure regulator (96.3–696 kPa pressure range, 4.5 kPa accuracy). Actual pressures were measured near the ports using Festo SPTE pressure sensors (96–1096 kPa pressure range) for input and output pressures and a Festo SPTW pressure sensor (0–1096 kPa pressure range) for the control pressure. Mass flow through the valve was measured by a Festo SFAH flow sensor (unidirectional, 100 L min^{-1} flow range) that was mounted between the the supplying pressure regulator and the input port. Pressure regulators and sensors were electrically interfaced via Beckhoff Ethercat I/O modules to a Speedgoat Unit real-time target machine. Components were connected using sections of hose with 1.2 and 2.5 mm inner diameter and standard push-in fittings. The available wall pressure was 746 kPa. This physical setup is shown in **Figure 5**.

4.3. Experimental Protocol

We commanded input pressures in the interval $p_{\text{in}}^{\text{cmd}} \in [121\,\text{kPa},\ 596\,\text{kPa}]$ in increments of 25 kPa and output pressures in the interval $p_{\text{out}}^{\text{cmd}} \in [96\,\text{kpa},\ p_{\text{in}}^{\text{cmd}} - 25\,\text{kPa}]$. For each of these combinations, control pressure $p_{\text{ctrl}}^{\text{cmd}}$ was initially commanded to be 596 kPa and then lowered to 96 kPa in decrements of 25 kPa. In total, data was collected at 4410 combinations of $p_{\text{in}}^{\text{cmd}}$, $p_{\text{out}}^{\text{cmd}}$, and $p_{\text{ctrl}}^{\text{cmd}}$. For each combination, we waited until the pressure stabilized, then held the commanded pressures for 2 s, and averaged all sensor readings over this period. In the flow sensor, we removed an observed bias by subtracting the minimally observed reading (which corresponded to a flow of 0 L min^{-1}) from all data.

For the input and control port, measured pressures were within 5 kPa of commanded pressures. For output pressures p_{out}, this held only at low and moderately high flow rates, because at very high flow rates, the downstream connection through the pressure regulator was not able to vent fast enough to atmosphere. In this regime, measured values deviated from commanded by up to 220 kPa. Using this protocol, we conducted the following four experiments: 1) We validated our model on an axi-symmetric valve. In addition to the overall goodness of the fit, we analyzed the valve's resistance in the fully open state as well as its closing characteristics. The results of these experiments are presented in Section 5.1; 2) We repeated this validation with a mirror-symmetric valve. Here, we accounted for the structural symmetry by testing forward and backward flows (Section 5.2); 3) We then expanded on our analysis to further investigate the dependency of the effective areas on flow magnitude and direction (Section 5.3); 4) Finally, we conducted a series of experiments in which we varied the valves' seat height h_{seat} (Section 5.4).

5. Results

5.1. Model Validation on the Axi-Symmetric Valve

To validate the model, we manufactured an axi-symmetric valve with diameters $d_{\text{in}} = 1.2\,\text{mm}$, $d_{\text{out}} = 6.5\,\text{mm}$, wall thickness

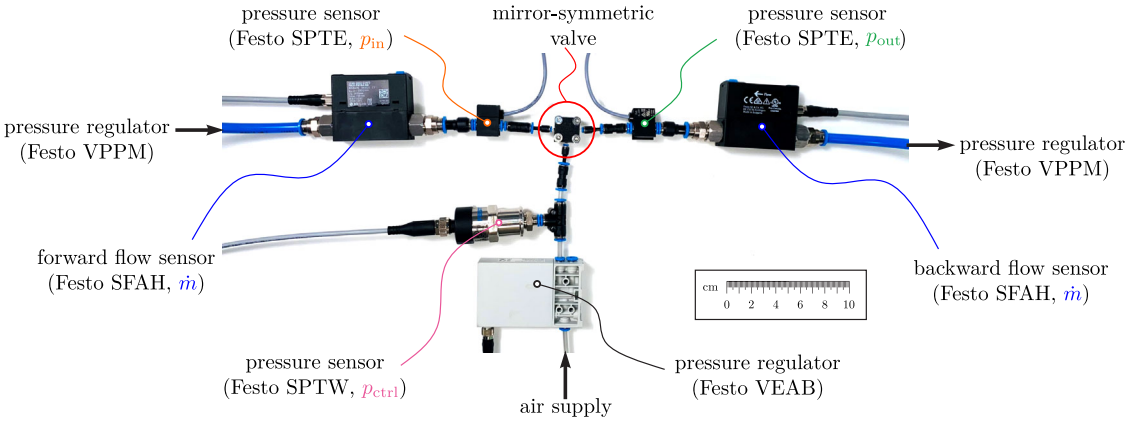

Figure 5. Experimental setup designed for measuring pressures and mass flow (here shown with a mirror-symmetric valve). The configuration includes three pressure sensors, three pressure regulators, and two unidirectional flow sensors. The flow sensor connected to the output port was only used for the mirror-symmetric valve, as the flow through the axi-symmetric valve was limited to a single direction.

$w_{seat} = 0.9\,mm$, and a designed seat height of $h_{seat} = 0.6\,mm$. It was connected to our experimental setup such that the input pressure was applied to the central chamber, as illustrated in Figure 2A.

5.1.1. Flow through the Open Valve

To validate whether our basic assumptions about an isothermal flow of a compressible fluid in a nearly constant Reynolds regime are correct, we first investigated the flow resistance of a fully open valve. To this end, we considered the 59 data points in which p_{ctrl} was set to atmospheric pressure ($p_{ctrl}^{cmd} = 96\,kPa$) and the sum of the commanded pressures for p_{in} and p_{out} was at least 900 kPa. This ensured that Δp was considerably larger than p_{trans} and hence the flow through the valve was dominated by R_f. These data points are shown in **Figure 6** and illustrate the linear relationships of $\sqrt{p_{in}^2 - p_{out}^2}$ as a function of $\dot{m}$. A linear fit without an intercept gave an estimated value for the resistance of $R_{open} = 0.558\,kPa\,mg^{-1}\,s$. This linear relationship describes the data with a coefficient of determination of $r^2 = 0.999$.

5.1.2. Linear Separability of Open and Closed States

We then identified the hyperplane separating open and closed valve states, by solving the quadratic program in Equation (21) with the MATLAB quadprog function.

For the identification, we chose $C = 0.1\,kPa^{-2}$ and set $\dot{m}_{min} = 1\,mg\,s^{-1}$, which was just above the noise that we observed for closed valve states. We obtained $a_{in} = 0.32$, $a_{out} = 0.71$, and $p_{close} = 96.42\,kPa$.

Figure 6 shows the resulting linear separation of open and closed valve states. Here, p_{ctrl} is plotted against $a_{in}p_{in} + a_{out}p_{out}$. For comparison, the 1232 data points with an open valve are marked blue, the remaining data points with

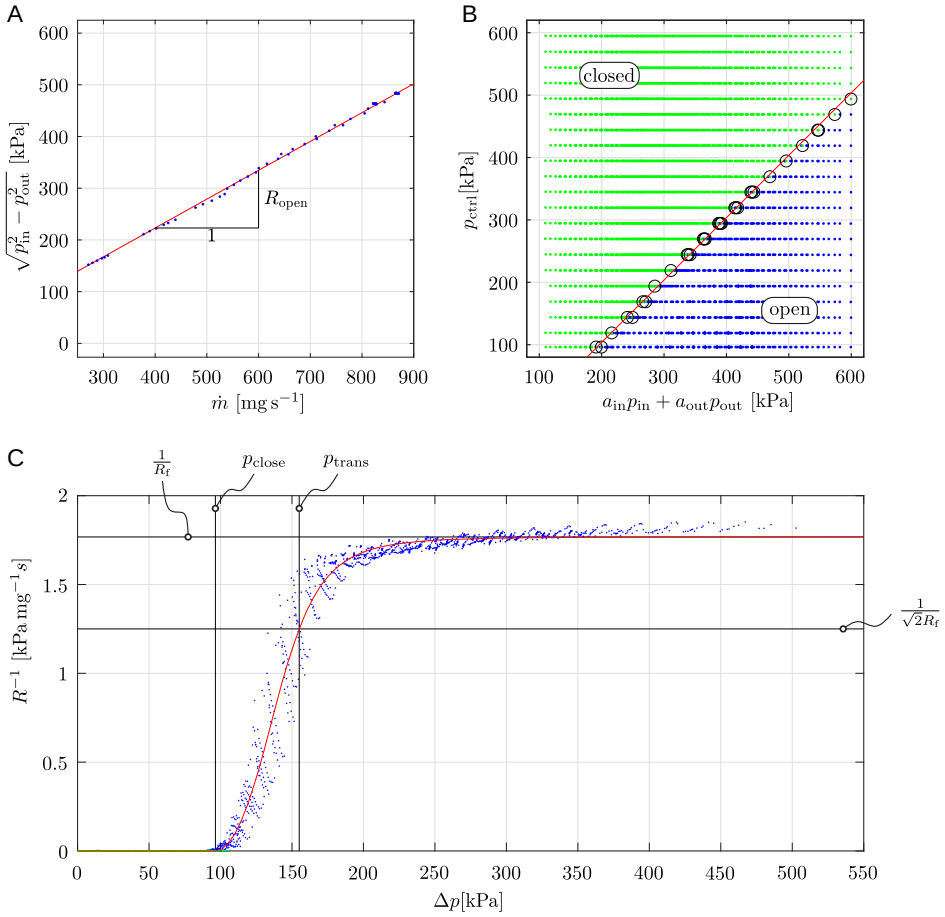

Figure 6. Model fitting results of the axi-symmetric valve: A) The relationship between mass flow $\dot{m}$ and difference of squared pressures $\sqrt{p_{in}^2 - p_{out}^2}$ for 59 experimental data points in which the valve was considered fully open ($p_{ctrl}^{cmd} = 96\,kPa$, $p_{in} + p_{out} \geq 900\,kPa$) is shown. The relationship is approximately linear ($r^2 = 0.999$), supporting the validity of Equation (4). B) Experimental data points are labeled as open (blue) and closed (green). The two conditions can be almost perfectly linearly separated as a function of pressure. Only 32 out of 4410 data points are miss-classified when we use the condition $\Delta p > p_{close}$ to identify open valves, with $\Delta p = a_{in}p_{in} + a_{out}p_{out} - p_{ctrl}$. Here, p_{ctrl} is plotted against $a_{in}p_{in} + a_{out}p_{out}$. C) Blue dots are measured values of $\frac{1}{R_i}$ versus $\Delta p = a_{in}p_{in,i} + a_{out}p_{out,i} - p_{ctrl,i}$, using the values of a_{in}, a_{out}, and p_{close} identified in Section 5.1.2. This data follows a functional relationship given by Equation (19). After fitting the parameters R_f, e, and p_{trans}, this function (shown in red) can explain $\frac{1}{R}$ with a RMSE of $0.099\,mg\,s^{-1}\,kPa^{-1}$.

a closed valve are marked green. Only 32 (marked with a circle) out of a total of 4410 data points were classified incorrectly and for those the maximum magnitude of deviation in terms of p_{ctrl} was 9.34 kPa.

5.1.3. Identification of Valve Resistance Characteristic

Figure 6 shows the measured values of $\frac{1}{R}$, that is of $\frac{\dot{m}}{\sqrt{p_{\text{in}}^2 - p_{\text{out}}^2}}$, as a function of Δp, using the values of a_{in}, a_{out}, and p_{close} identified above. While there is some spread of the data, the $\frac{1}{R}$ values generally follow a functional relationship with respect to Δp as given by Equation (19). We identified $R_f = 0.566\,\text{kPa}\,\text{mg}^{-1}\,\text{s}$, $e = 1.99$, and $p_{\text{trans}} = 155.1\,\text{kPa}$. For R_f this is almost identical to the value of R_{open} identified for the fully open valve above. The exponent e was close to the expected value. The root mean square error (RMSE) between the predicted and measured values of $\frac{1}{R}$ was $0.099\,\text{mg}\,\text{s}^{-1}\,\text{kPa}^{-1}$, compared to a maximal inverse resistance of $1.85\,\text{mg}\,\text{s}^{-1}\,\text{kPa}^{-1}$.

5.1.4. Overall Goodness of Fit

The model identified above was able to predict the flow across all 4410 data points with RMSE of $16.8\,\text{mg}\,\text{s}^{-1}$. One could argue that this value is a bit skewed, as it contains 3178 data points in which the valve is completely closed. If we only consider the 1232 data points in which flow is present (i.e., with $\dot{m}_i > \dot{m}_{\text{min}}$), the RMSE is $31.7\,\text{mg}\,\text{s}^{-1}$. This is about 4% of the maximally observed flow of $871.1\,\text{mg}\,\text{s}^{-1}$. Part of the data for a commanded input pressure of $p_{\text{in}}^{\text{cmd}} = 396\,\text{kPa}$ is shown in **Figure 7**A, with the prediction error being shown in Figure 7B.

5.2. Model Validation on the Mirror-Symmetric Valve

We further manufactured a mirror-symmetric valve with diameter $d_{\text{io}} = 6.5\,\text{mm}$, wall thickness $w_{\text{seat}} = 0.90\,\text{mm}$, and seat height $h_{\text{seat}} = 0\,\text{mm}$. This valve was tested using the protocol described in Section 4.2. It can support flow in both directions, and the input pressure p_{in} was first applied to port 1 of the valve (forward flow) and then applied to port 2 (backward flow). The parameters identified for both tests are given in **Table 1**. As expected from the symmetry, the direction of flow does not alter the valve's parameters. However, one needs to keep in mind that the effective area a_{in} is always associated with the port that is considered the input, that is, the port with the higher pressure. That means, if the valve is used in bidirectional flow with pressure p_1 applied to port 1 and pressure p_2 applied to port 2, we have to compute Δp as

$$\Delta p = \begin{cases} a_{\text{in}} p_1 + a_{\text{out}} p_2 - p_{\text{ctrl}}, & p_1 > p_2 \\ a_{\text{in}} p_2 + a_{\text{out}} p_1 - p_{\text{ctrl}}, & p_1 < p_2 \end{cases} \tag{25}$$

Table 1. Parameters identified for a mirror-symmetric valve when installed in two different flow directions.

		Forward	Backward
a_{in}	[−]	0.578	0.588
a_{out}	[−]	0.459	0.439
p_{close}	[kPa]	21.860	19.520
R_f	[kPa mg^{-1} s]	0.400	0.395
e	[−]	1.650	1.620
p_{trans}	[kPa]	96.020	93.440

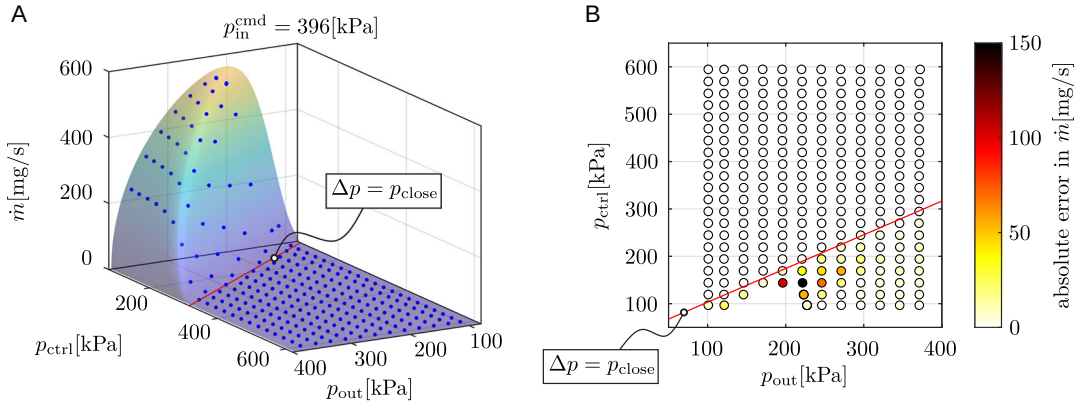

Figure 7. Model prediction versus measurements of the axi-symmetric valve for $p_{\text{in}}^{\text{cmd}} = 396\,\text{kPa}$. A) Exemplary values of mass flow as a function of p_{out} and p_{ctrl} are shown for a commanded input pressure of $p_{\text{in}}^{\text{cmd}} = 396\,\text{kPa}$. This data (blue dots) is compared to the model prediction shown as a shaded surface. Clearly visible are a saturation area (at the lowest values of p_{ctrl}) in which flow depends primarily on p_{out} and is characterized by the fixed resistance R_f, the flat area in which the valve is fully closed, and the transition in between the two which is characterized by the parameters p_{close}, p_{trans}, and e. The red line shown in both figures indicates the predicted separation between open and closed valve states, given by $\Delta p = p_{\text{close}}$. B) Error between the measured data (blue dots) and the model prediction (shaded surface) shown in A). Overall (i.e., not only for $p_{\text{in}}^{\text{cmd}} = 396\,\text{kPa}$), mass flow is predicted with RMSE of $16.8\,\text{mg}\,\text{s}^{-1}$. If we only consider data in which the valve is open, the RMSE is $31.7\,\text{mg}\,\text{s}^{-1}$. The gap in the data for low p_{ctrl} and values of p_{out} around 175 kPa appear because the servo valve controlling the output pressure was not able to vent the resulting air flow to atmosphere. That is, when p_{out} was commanded to 221 kPa and lower, the actual pressure (which was measured and used in the evaluation) never went below 227 kPa. This effect disappears for values of $p_{\text{out}} < 121\,\text{kpa}$, as the valve is closing and the flow reduced.

Overall, the model of the mirror-symmetric valve was able to predict the flow across all 4410 data points with RMSE of 29.3 mg s^{-1} in the forward direction (33 mg s^{-1} in the backward direction). If we only consider the 2247 (2262) data points in which flow was present, the RMSE is 41 mg s^{-1} (46.1 mg s^{-1}). For both directions, this is about 4% of the maximally observed flow of 1052 mg s^{-1} (1064 mg s^{-1}).

5.3. Dependency of the Effective Areas on Flow Magnitude and Direction

An important assumption in our model is that the resistance R is a function of the equivalent pressure difference Δp and that this quantity is linear in the three applied pressures p_{in}, p_{out}, and p_{ctrl}. Moreover, we assumed that the relative effective areas a_{in} and a_{out} in Equation (16) do not depend on the magnitude of flow.

We saw in the previous section that there is a directional dependency that arises because the flow of fluid causes the input pressure to act on the membrane over an area that is larger than what is geometrically associated with the input. For instance, the in the axi-symmetric valve, the cross-sectional area of the inflow chamber is $A_{\text{in}}^{\text{geom.}} = \frac{\pi}{4}(d_{\text{in}} + w_{\text{seat}})^2 = 3.5\,\text{mm}^2$, the cross-sectional area of the outflow chamber is $A_{\text{out}}^{\text{geom.}} = \frac{\pi}{4} d_{\text{out}}^2 - A_{\text{in}}^{\text{geom.}} = 29.7\,\text{mm}^2$, and the cross-sectional area of the control chamber is $A_{\text{ctrl}}^{\text{geom.}} = \frac{\pi}{4} d_{\text{out}}^2 = 33.2\,\text{mm}^2$. We can perform a normalization of these areas similar to the one in Equation (16), yielding $a_{\text{in}}^{\text{geom.}} = \frac{A_{\text{in}}^{\text{geom.}}}{A_{\text{ctrl}}^{\text{geom.}}} = 0.104$ and $a_{\text{out}}^{\text{geom.}} = \frac{A_{\text{out}}^{\text{geom.}}}{A_{\text{ctrl}}^{\text{geom.}}} = 0.896$. These relative geometrical areas can be compared to the relative effective areas $a_{\text{in}} = 0.32$ and $a_{\text{out}} = 0.71$. Due to the direction of flow, the relative effective area of the input is enlarged of the output reduced. In the mirror-symmetric valve, we get a similar effect with $A_{\text{in}}^{\text{geom.}} = A_{\text{out}}^{\text{geom.}} = \frac{\pi}{8} d_{\text{io}}^2 = 14.2\,\text{mm}^2$ and $A_{\text{ctrl}}^{\text{geom.}} = \frac{\pi}{8} d_{\text{io}}^2 = 28.3\,\text{mm}^2$. That is, $a_{\text{in}}^{\text{geom.}} = a_{\text{out}}^{\text{geom.}} = 0.5$. Compared with the relative effective areas (Table 1), we again see a shift that increases the relative effective area associated with the input and decreases the relative effective area associated with the output.

To validate the assumption that the relative effective areas do not depend on the magnitude of the flow, we computed the separating hyperplane of Equation (20)–(22) not only for a minimal threshold $\dot{m}_{\text{min}}$, but also for a range of inverse resistance values. Thus, we replaced the classification in Equation (20) with

$$y_i = \begin{cases} +1, & \frac{1}{R_i} > \frac{1}{R_{\text{sep}}} \\ -1, & \frac{1}{R_i} \leq \frac{1}{R_{\text{sep}}} \end{cases} \tag{26}$$

where R_i was determined from the recorded data via Equation (4). That is, we linearly separate our data in the pressure space according to whether the resulting inverse resistance is above or below a given threshold $\frac{1}{R_{\text{sep}}}$, where we varied $\frac{1}{R_{\text{sep}}}$ in the range from 0.005 mg s^{-1} kPa^{-1} to $\frac{1}{R_{\text{f}}}$.

The resulting effective areas $\tilde{a}_{\text{in}}(R_{\text{sep}})$ and $\tilde{a}_{\text{out}}(R_{\text{sep}})$ are shown in **Figure 8**, where they are also compared to the constant values a_{in} and a_{out} identified in Section 5.1.2. For inverse resistances of up to $\frac{\sqrt{2}}{2}\frac{1}{R_{\text{f}}}$, the resulting relative effective areas $\tilde{a}_{\text{in}}$ and $\tilde{a}_{\text{out}}$ are fairly constant. Furthermore, when using the values of a_{in} and a_{out} identified in Section 5.1.2 and just adapting p_{close}, the number of miss-classified data points is below 1% within this range. That is, the values of a_{in} and a_{out}, identified at the onset of flow, are valid over a wide range of resistance values (Figure 8).

For resistance values higher than $\frac{\sqrt{2}}{2}\frac{1}{R_{\text{f}}}$, the linear separation is no longer feasible. This is not surprising, as in this flow regime the fixed resistance that is inherent to the conduits connected to the input and output ports starts to dominate.

5.4. Parametric Variations

To understand the role of the model parameters, we further conducted a parameter study in which we manufactured 22 axi-symmetric valves and varied the seat height h_{seat} between

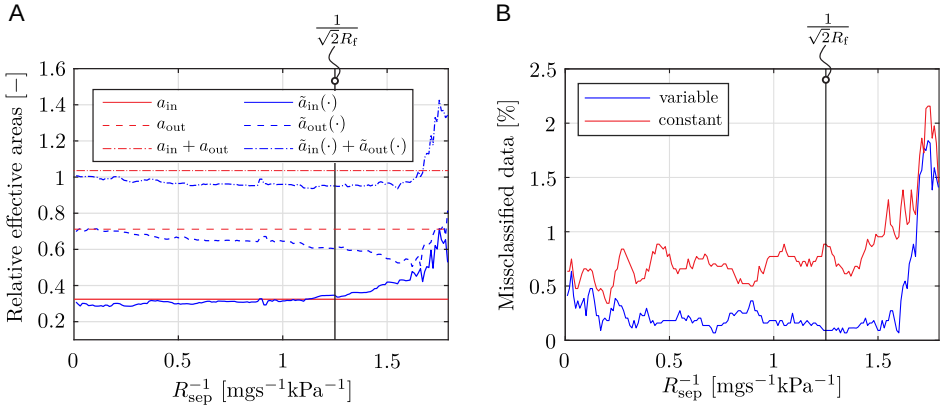

Figure 8. A) Blue indicates the relative effective areas $\tilde{a}_{\text{in}}$ and $\tilde{a}_{\text{out}}$ that were obtained by linearly separating the data in the pressure space between data points with an inverse resistance larger and smaller than $\frac{1}{\sqrt{2}R_{\text{f}}}$. These values are similar for a wide range of values for $\frac{1}{R_{\text{sep}}}$ and thus for a wide range of flows. Over this range, they are comparable to the constant values a_{in} and a_{out} obtained when separating the data according to open/close states as given by Equation (20) (horizontal red lines). B) The fraction of data points that are miss-classified via this separation is below 1% (blue line), even if the constant a_{in} and a_{out} are used (red line).

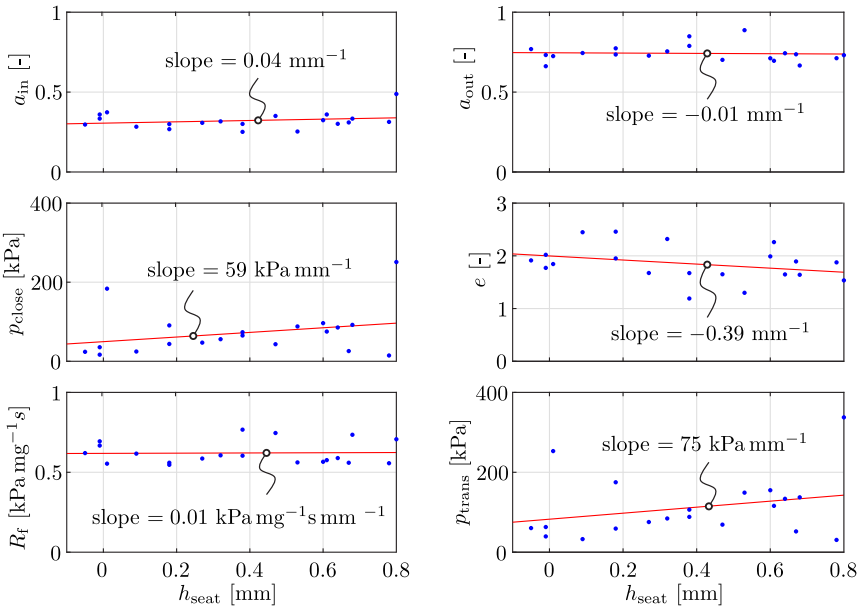

Figure 9. Model parameters as a function of measured seat height, for a series of 20 axi-symmetric valves. To visualize trends in the data, we also show a linear least-squares fit with an intercept. As one would expect, the variation in seat height primarily influences the opening characteristic of the valve as it is expressed by the closing pressure p_{close}, the transition pressure p_{close}, and the exponente.

0 mm and 0.8 mm in increments of 0.1 mm. Each seat height was manufactured twice, with the exception of the design seat height of 0 mm, which was manufactured 6 times to allow for the evaluation of data consistency. Two of the valves (with h_{seat} 0 mm and 0.8 mm) showed leakage (our exclusion criterion for leakage was a flow larger than $\dot{m}_{min}$ at the conditions $p_{ctrl}^{cmd} = 596\,kPa$ and $p_{out}^{cmd} < p_{in}^{cmd} = 496\,kPa$, for which the valve should be fully closed) and were excluded from the dataset. After manufacturing, actual seat height was measured with a digital caliper.

For each valve, we conducted an experimental data collection and identified the six parameters as described in Section 4. The resulting values are shown in **Figure 9** as a function of measured seat height. To highlight trends in the data, we also show in linear least-squares fit with an intercept together with the data. While a_{in}, a_{out}, R_f, and e are only marginally affected by seat height, the pressures p_{close} and p_{trans} show a dependency, highlighting how the seat height primarily influences the opening characteristic of the valve.

6. Applications

In the following sections, we showcase the application of the fluid-driven membrane valves along with the corresponding mathematical model in two real-world scenarios. We demonstrate the flow amplification properties of the membrane valves in Section 6.1, followed by the presentation of a fluidic osciallator circuit in Section 6.2.

6.1. Flow Amplification

To tackle the piping problem, locally embedded valves can be used to drive pneumatic actuators using a single-fluid supply line and thin control channels (see Figure 1). For fluid-driven valves, this requires a flow amplification; that is, a small flow in the control channel (and an associated change in pressure) results in a high flow rate through the valve which is needed to rapidly inflate and deflate larger pneumatic actuators. This increases the bandwidth of the system and improves performance.

We conducted an experiment in which we controlled the inflation of a single McKibben actuator (**Figure 10**A) and compared the performance of axi-symmetric fluid-driven membrane valves with Clippard electronic valves (1 mm orifice size). The Clippard valves have a smaller footprint than the membrane valves, with a weight of 6 g and a volume of 3.5 cm^3 (including the fluidic manifold) compared to 17 g and 11.5 cm^3 of the membrane valves. However, it should be noted that the Clippard valves are an optimized commercial product while the membrane valves are a first prototype. Figure 10B showcases the results of the periodic contraction of a McKibben actuator. Both valves result in very similar inflation and deflation times, highlighting the competitiveness of our valves compared to off-the-shelf electronic valves. A video of this experiment is provided in the supplemental materials.

6.2. Oscillator Circuit

The fact that the flow through a fluid-driven membrane valve is dependent on the pressure at the output port p_{out} gives rise to a second application, the creation of a fluidic oscillator. With the circuit shown in **Figure 11**A, an adjustable pressure oscillation can be achieved from a constant pressure source, using only a single valve, two resistances, and a volume acting as a pneumatic capacitor. Such oscillators have been proposed in the past, using a different type of valve that was based on kinked tubes.[22] They can be used to autonomously drive pneumatic actuators, for

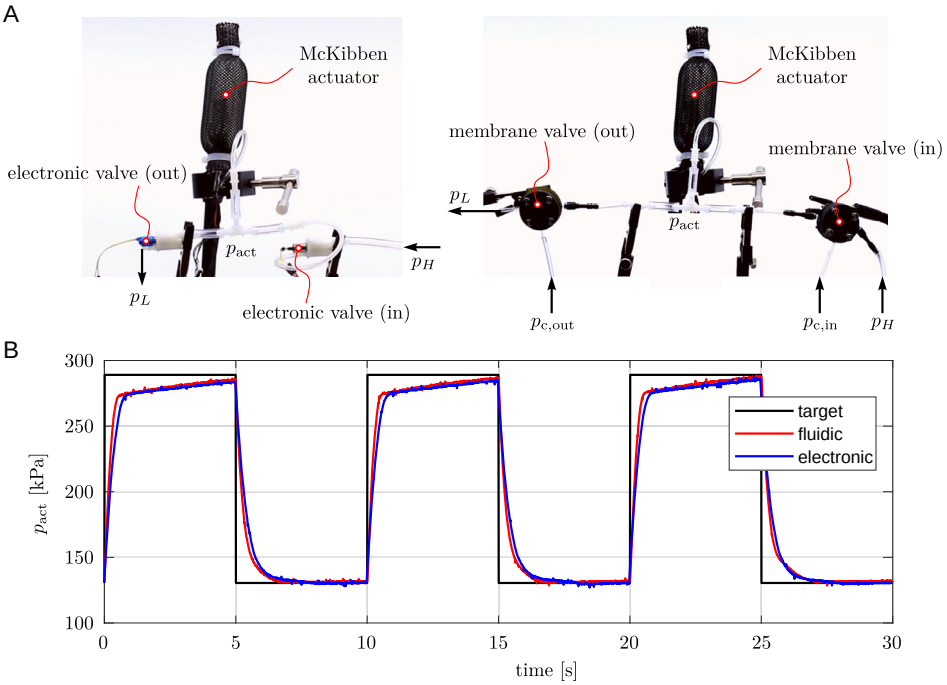

Figure 10. A) The flow amplification setup used to inflate a 10 cm-long McKibben actuator. The Clippard electronic valves are utilized in the left picture, and the axi-symmetric membrane valves are used in the right picture. A high-pressure source of $p_H = 289$ kPa was provided to the (in) valves, and the McKibben vents to a low-pressure source of $p_L = 120$ kPa through the (out) valves. The sensor measuring the actuator pressure p_{act} is embedded in the McKibben itself. B) 30 s-long experiment run of both setups. Here, the McKibben is cycled between p_H and p_L in 5 s intervals. The actuator pressure p_{act} from the fluid-driven membrane valve is shown in red, and from the Clippard electronic valve in blue. A slight performance advantage can be seen by the fluidic valve, with faster pressure increases and decreases, showing higher mass flow rates.

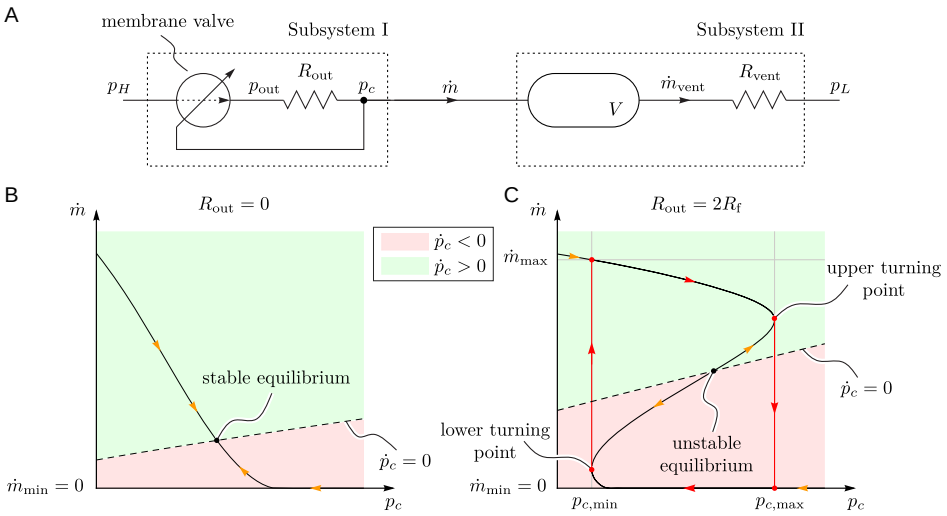

Figure 11. A) Schematic of an oscillator circuit, consisting of a membrane valve, a fixed volume, and two resistors. For analysis, we divide the circuit into two subsystems I and II. B,C), the admissible stationary values of p_c and $\dot{m}$ in Subsystem I are shown as black lines and the sign of $\dot{p}_c$, as it results from the dynamics in Subsystem II, via the colored areas. By combining the solutions of Subsystem I with the change of p_c as it follows from Subsystem II, we can obtain the dynamics of the entire circuit. In (B), for $R_{out} = 0$, we see a convergence to a stable equilibrium in mass flow and pressure. By increasing the output resistance to $R_{out} = 2R_f$, we see the creation of a limit cycle in (C). The solution follows the top (bottom) branch of admissible solutions to the right (left) until it hits the upper (lower) turning point, where it jumps to the other solution branch. The cycle is illustrated with red arrows showing the direction of travel.

example, to create a periodic gait for locomotion.[31] Using the membrane valves presented in this article can potentially lead to a much more compact design of such circuits.

To understand the function of this oscillator, we first focus on Subsystem I in Figure 11A. Here, the input of the membrane valve is directly connected to a high-pressure source p_H. The output of the valve is connected via a pneumatic resistor R_{out} to the pressure p_c, which is also fed into the control port of the valve. Due to the resistor, the output pressure at the valve p_{out} depends on the mass flow through the valve, according to

$$p_{out} = \sqrt{\dot{m}^2 R_{out}^2 + p_c^2} \tag{27}$$

Substituting this relationship into Equation (19) leads to

$$\dot{m} = \begin{cases} 0 & , \quad \Delta p \leq p_{close} \\ \dfrac{\sqrt{p_H^2 - p_c^2 - \dot{m}^2 R_{out}^2}}{R_f \sqrt{1 + \left(\frac{\Delta p - p_{close}}{p_{trans} - p_{close}}\right)^{-2e}}} & , \quad \Delta p > p_{close} \end{cases} \tag{28}$$

with $\Delta p = a_{in} p_H + a_{out}\sqrt{\dot{m}^2 R_{out}^2 + p_c^2} - p_c$ being the equivalent pressure difference of Equation (13) in this circuit. Note that $\dot{m}$ now also appears on the right hand side of the equation, leading to an implicit relationship between the pressure p_c and the flow rate $\dot{m}$.

The solutions to this equation (i.e., the admissible values of p_c and $\dot{m}$ for a constant value of p_H) are shown as black lines in Figure 11B,C. For $R_{out} = 0$ (Figure 11B), the relationship of p_c and $\dot{m}$ is monotonic. As p_c is increased, $\dot{m}$ is diminished, until the valve closes completely. However, for $R_{out} = 2R_f$ (Figure 11C), one can observe that the solution curve has two turning points and that different mass flow values are possible for the same value of p_c. This hysteresis is caused by the fact that in a membrane valve the output pressure p_{out} pushes against p_{ctrl} from the other side of the membrane. If the valve is open, the mass flow $\dot{m}$ through the resistor causes p_{out} to rise above p_c, which pushes the valve open as described before. In contrast, if no flow is present p_{out} will drop to the value of p_c and this effect vanishes.

In Subsystem II, the fluid volume acts as an integrator, whose dynamics can be obtained by taking the time derivative

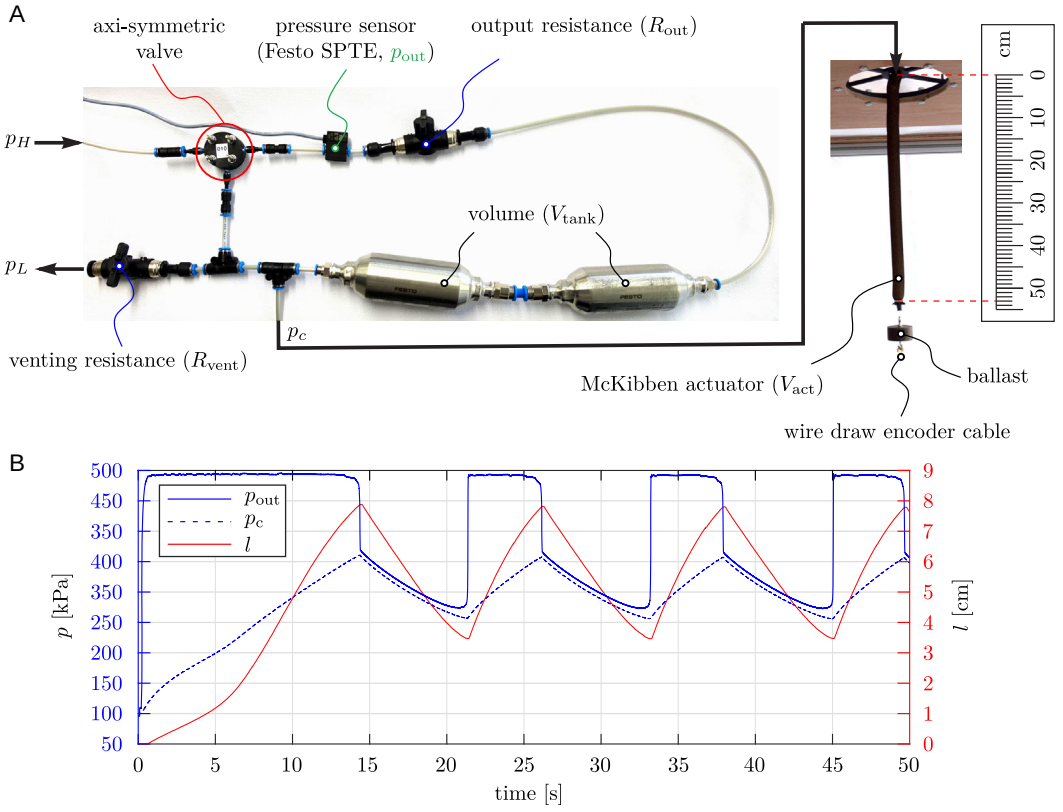

Figure 12. A) The experimental setup of an oscillator circuit. A constant supply pressure ($p_H = 496$ kPa) is fed into the input port of an axi-symmetric membrane valve. After passing through an adjustable resistance R_{out}, the air flows into two Festo air reservoirs (total volume $V_{tank} = 200$ mL) acting as a pneumatic capacitor. The tanks are connected to the control port of the membrane valve and a McKibben actuator and are vented to atmospheric pressure ($p_L = 96$ kPa) through a second adjustable resistance R_{vent}. We used ball valves as variable resistances which were manually adjusted to create the pressure oscillation cycle. Two Festo SPTE pressure sensors measured the pressures p_{out} and p_c (note that the sensor for p_c was mounted near the actuator and is not shown in this figure). The vertical McKibben actuator is tensioned by a weight of 200 g and its contraction is measured by a wire draw encoder. The result of a 50 s long-experiment run, with the pressures plotted blue, and the contraction of the McKibben in red, is shown in B).

of the ideal gas law and solving for the pressure change p_c inside the volume V:

$$\dot{p}_c = \frac{R_{gas}T}{MV}\left(\dot{m} - \frac{\sqrt{p_c^2 - p_L^2}}{R_{vent}}\right) \tag{29}$$

Here, $\dot{m}$ is the mass flow into the volume coming from the membrane valve and $\frac{\sqrt{p_c^2-p_L^2}}{R_{vent}}$ is the mass flow venting to a low pressure p_L through another pneumatic resistor R_{vent}. The important aspect is whether this derivative is positive or negative; that is, whether the mass flow into the volume is larger or smaller than the mass flow out of the volume. These different regimes have been colored in Figure 11B,C, with positive values being green and negative values being red.

To analyze the complete circuit depicted in Figure 11A, we have to combine the two solutions of Subsystems I and II. Visually, this means that the solution must evolve along the black lines as dictated by Subsystem I, and it must move toward the right in the green areas and toward the left in the red areas. For $R_{out} = 0$ (Figure 11B), the solution will quickly converge to a stable equilibrium, in which the valve is partly open and the pressure in the volume remains constant (orange arrows). For $R_{out} = 2R_f$ (Figure 11C), the solution will evolve along the top branch (valve open) toward the right, until it hits the upper turning point and jumps to the bottom branch (valve closed). On this branch, the solution is now moving toward the left, until it hits the lower turning point and jumps back to the top branch (red arrows). The detailed behavior of this limit cycle depends on the location of the two turning points: the lower one defines the minimum oscillation pressure $p_{c,min}$ and the upper one the maximum pressure $p_{c,max}$. These locations are primarily influenced by the resistance R_{out}. The venting resistance R_{vent} must be tuned such that for the top branch, the control pressure increases ($\dot{p}_c > 0$) and for the bottom branch the control pressure decreases ($\dot{p}_c < 0$). Finally, the oscillation period depends primarily on the fluid volume V. A larger volume leads to a longer filling and emptying cycle, which leads to a longer oscillation period. One should note that solutions also exist on the middle branch, but quickly diverge from an unstable equilibrium at $\dot{p}_c = 0$ to join the limit cycle (orange arrows).

To validate these theoretical findings, we implemented this circuit to power the oscillating contraction of a single McKibben actuator (**Figure 12**A). To this end, a McKibben muscle of relaxed length $\hat{l} = 53$ cm was connected in parallel to two tanks with a combined volume of $V_{tank} = 200$ mL. The actuator was set up vertically to pull up a ballast weight of 200 g. This contraction was measured via a SICK wire draw encoder cable attached to the base of the ballast weight. The used membrane valve had a high seat height of $h_{seat} = 0.7$ mm to accentuate the hysteresis effect. Slightly opened manual shut-off valves were used for the two resistances. A constant pressure of $p_H = 496$ kPa was supplied to the circuit, and it was vented to atmospheric pressure of $p_L = 96$ kPa. The contractions of the McKibben muscle alongside both valve output pressure p_{out} and feedback pressure p_c were measured during the experiment. Figure 12B shows the results of a 50 s long experimental run. A video of this experiment is provided in the supplemental materials.

7. Discussion & Conclusion

As primary contribution, this article introduced a physics-based model that characterizes the flow–pressure relationship of small-scale high-flow fluid-driven membrane valves. We developed two such valves and, in a set of experiments, were able to show that our model was able to predict flow magnitudes within 4% of measured values. The model also reliably identified the onset of flow, with less then 1% of data points being miss-classified. Moreover, we showcased our valves' capabilities in fluid amplification and the model's ability to predict an oscillation in pressure in a fluidic circuit. The model relies on six parameters, all of which have a clear and unambiguous physical meaning, which enhances the interpretability of the model and makes it applicable in a design context. Among these parameters, the fixed resistance R_f and the valve closing pressure p_{close} are probably the most important in terms of sizing a valve for a certain flow rate and giving it a desired behavior within a fluid network. We describe a systematic two-step characterization process, which allowed us to reliably identify all six parameters from experimental data.

A number of physics-based assumptions went into the development of the model and we carefully validated each of these individually. As a general resistance model, we first assumed a linear relationship between the squares of flow and the differences in squares of pressure. This relationship corresponds very well to experimental data ($r^2 = 0.999$), as shown in Figure 6. Notably, the resistance value derived from the linear fit in this figure also matched the value for R_f that was identified later for the full model. We also found that the quadratic terms used in Equation (4) were clearly superior to modeling pressure drop as being directly proportional to flow. Our second assumption was a linear relationship in the equivalent pressure difference Δp, based on the relative effective areas introduced in Equation (16). In our model, these equivalent areas only depend on the direction of flow, not on its magnitude. As shown in Figure 8, this assumption holds reasonably well for different flow values. Finally, we assumed that a functional relationship exists between the equivalent pressure difference Δp and the resulting variable resistance R_v across the valve. The quality of this assumption can best be assessed in Figure 6, where the data points for $\frac{1}{R}$ can be seen to form such a functional relationship. For this relationship, we proposed an exponential function, based on insights from flow resistance through cylindrical channels.

Equation (13) highlights that changes in the output pressure p_{out} affect the equivalent pressure difference Δp and thus the flow $\dot{m}$. This has interesting consequences when using such valves in a fluidic system with additional components. For example, if the output is connected to a fluidic capacitance, that is, an enclosed volume such as a soft robotic actuator, this can lead to positive feedback: flow into such a capacitance will lead to an increase in pressure, which will increase Δp and will in turn further increase the flow. Such an effect may not be limited to closed volumes, but may also apply to a downstream volume that is vented through a resistance. In such a configuration, an increase in flow can also lead to an increase in pressure, further opening the valve in a positive feedback cycle. As the opposite effect occurs when flow is reduced, this may lead to a hysteretic

behavior of the overall system. These phenomena warrant careful consideration in future iterations of such a valve model, in particular the question to what degree such effects may occur within the valve itself.

In terms of potential applications, the model presented in this article lays the groundwork for predicting the behavior of fluid-driven actuators and robots and can provide insights for the control and design of soft robotic systems. Potential control applications include the determination of gains for classical feedback-loops, the ability to use model predictive control strategies, and the use of open-loop control in situations in which feedback is unavailable. The model can not only serve as a tool for understanding the behavior of soft robots but also for shaping that behavior. That is, the physics-based parameters can assist with guiding the design of valves for a given application. For example, if a certain logical behavior is desired from an interconnected fluid network, the valve-closing pressure p_{close} becomes an important parameter, as it essentially determines the pressure gain of a particular valve. Similarly, the sizes of the relative effective areas a_{in} and a_{out} determine how pressure changes within the network influence the flow through a particular valve. The fixed resistance R_{f} describes the size (in terms of maximum flow) of the valve. Finally, the exponent e and the transition pressure p_{trans} determine the responsiveness of the valve and thus its temporal behavior in a dynamic context. That is, they play an important role in systems in which feedback mechanisms are present. This physical interpretability makes the formulation presented in this article a useful tool for a model/simulation-based design approach.

Though the valves that we modeled and tested in this article are structurally similar to valves used in traditional microfluidic systems,[19,21,26,32] they were specifically developed for applications in soft robotic systems. This primarily concerns the scale of the valves. In order to drive soft fluidic actuators they have to regulate a much larger magnitude of flow than that typically encountered in microfluidic circuits. We also introduced an axi-symmetric valve design that differs from the mirror symmetric valves found in conventional microfluidic systems.[17,18,24] A primary benefit of the axi-symmetric design is that it allows for a large variation of the seat height without compromising the ability to seal the flow. While the primary focus of this article has been on model validation, the inherent capabilities of these valves are clearly evident in the magnitude of flow achieved and the pressure gains that we observed.

The flow through the valves studied in this article is targeted to meet the supply requirements of typical soft fluidic actuators. The maximal flow rate that we observed in our experiments was 871.1 mg s^{-1} for an input pressure of 596.1 kPa and an output pressure of 349.1 kPa. This corresponds to a normal nominal flow of 40.4 L min^{-1}. Taking the soft actuator experiments from another study[33] as an example, the flow through a fully open axi-symmetric valve with resistance $R_{\text{f}} = 0.566\,\text{kPa}\,\text{mg}^{-1}\,\text{s}$ would fill a 173 mm-long McKibben actuator with an inner diameter of 20 mm from atmospheric pressure to a gauge pressure of 200 kPa in less than 131 ms (using a supply gauge pressure of 500 kPa).

These values are compared to a number of studies with respect to internal resistance, size, and weight in **Table 2**.

Table 2. Comparison of valve specifications.

Valve Type	Resistance [kPa mg^{-1} s]	Size [cm^3]	Weight [g]
Axi-Symmetric Membrane Valve	0.566	11.5	17
Mirror-Symmetric Membrane Valve	0.400	5.3	11
Festo VPPM	0.042	300.4	400
Festo VEAB	1.164	92.6	70
Clippard Electronic Valve (1 mm orifice)	7.752	3.5	6
Offchip Microvalve for Microfluidics	33.059	3.3	3

The comparison includes the Festo VPPM servo valves that were used in our experimental setup to supply the input and output ports, the Festo VEAB valve used to supply the control port, the Clippard electronic valves (1 mm orifice size) used in the flow amplification experiment in Section 6.1, and offchip microvalves used for microfluidics.[34] A considerable reduction in size and weight is achieved by our membrane valves compared to the Festo valves, and compared to the Clippard electronic valves, we achieve a lower pneumatic resistance. Here, the resistance of the Clippard valves was calculated from the information provided on their data sheet. It should be noted that the results of Section 6.1 do not fully reflect these computed values, as we observed similar inflation and deflation times. A potential explanation could be that either the pneumatic resistance of the tubing in the experimental setup dominates over the resistance of the valves or that the values provided in the data sheet are conservative.

With this low mass and volume, our membrane valves could be directly embedded into the structure of a soft-robotic system, thereby providing a promising solution for tackling the piping problem. In the process, it is likely that further mass and volume savings can be achieved by combining multiple valves in the same 3D-printed substrate. This is partly shown in Section 6.1 with promising results; however, more work can be done to remove unnecessary piping and actually embed the valves in the actuator, driving down the pneumatic resistance of the overall circuit and enabling faster inflation times.

When used as a logical component in a fluidic network, such as for example an inverter, another important property of a valve is its pressure gain,[21] that is, its ability to switch a high-pressure flow with a smaller control pressure. Pressure gain allows cascading logical elements as it can compensate for pressure loss in the interconnecting resistances. In our valve model, such pressure gain is reflected in the closing pressure p_{close}. The condition for a closed valve is $\Delta p \leq p_{\text{close}}$ (Equation (19)), which we can express as $p_{\text{ctrl}} + p_{\text{close}} \geq a_{\text{in}} p_{\text{in}} + a_{\text{out}} p_{\text{out}}$. That is, p_{close} directly reduces the control pressure p_{ctrl} that is needed to close the valve. The pressure needed to close the valve can be influenced by the seat height of a valve, and in our experiments we were able to achieve values of p_{close} in excess of 100 kPa. Furthermore, we demonstrate the ability to create periodic oscillations in pressure with a constant pressure source, which can be used as a reference clock in fluid logic circuits, or used to drive periodic motions, in Section 6.2.

For future work, we see avenues for extending our model to encompass noncompressible fluids and opportunities to apply and validate our approach across other structural valve designs. Potential extensions of our formulation to further improve the predictive capabilities of the model will likely consider the pressure drop across resistances within the valve and how such a pressure drop will influence the deformation of the membrane. In the current model, such effects are essentially lumped into the size of the relative effective areas a_{in} and a_{out}, which do not necessarily reflect the geometric dimensions of the valve (see Section 5.3). Considering such effects more explicitly, modeling the interior of the valve as resistances and capacitances connected in series will likely improve the predictive capabilities of the model across a range of flows.

The long-term goal of our research is to enable hyperactuated soft robotic systems which will be driven by a distributed and fluid-driven valve network that is directly embedded in the substructure of the robot. The modeling and the valves presented in this article will play a pivotal role in this ongoing journey. In particular the physical interpretability of the model makes it a powerful tool for the realization of advanced soft robotic systems that combine the strengths of fluid logic with flow amplification.

Supporting Information

Supporting Information is available from the Wiley Online Library or from the author.

Acknowledgements

T.D. and N.V. contributed equally to this work. This work was supported by the CZS Prisma Program of the Carl-Zeiss-Stiftung and by the Deutsche Forschungsgemeinschaft (DFG, German Research Foundation) under Germany's Excellence Strategy – EXC-2075–390740016. The authors acknowledge the support by the Stuttgart Center for Simulation Science (SimTech). In addition, Toyota Research Institute provided funds to support this work in its early phases. The authors also would like to acknowledge Runze Zuo (Mechanical Engineering, University of Michigan) for assistance in the setup and data collection of the flow amplification experiment.

Open Access funding enabled and organized by Projekt DEAL.

Conflict of Interest

The authors declare no conflict of interest.

Data Availability Statement

The data that support the findings of this study are available from the corresponding author upon reasonable request.

Keywords

fluid-driven valves, high-flow, modeling, soft robots

Received: December 13, 2023
Revised: March 22, 2024
Published online: May 16, 2024

[1] F. Ilievski, A. D. Mazzeo, R. F. Shepherd, X. Chen, G. M. Whitesides, *Angew. Chem., Int. Ed.* **2011**, *50*, 1890.
[2] C. Majidi, *Soft Rob.* **2014**, *1*, 5.
[3] D. Rus, M. T. Tolley, *Nature* **2015**, *521*, 467.
[4] R. F. Shepherd, F. Ilievski, W. Choi, S. A. Morin, A. A. Stokes, A. D. Mazzeo, X. Chen, M. Wang, G. M. Whitesides, *Proc. Natl. Acad. Sci.* **2011**, *108*, 20400.
[5] B. Mosadegh, P. Polygerinos, C. Keplinger, S. Wennstedt, R. F. Shepherd, U. Gupta, J. Shim, K. Bertoldi, C. J. Walsh, G. M. Whitesides, *Adv. Funct. Mater.* **2014**, *24*, 2163.
[6] D. Bruder, A. Sedal, R. Vasudevan, C. D. Remy, *IEEE Rob. Autom. Lett.* **2018**, *3*, 3999.
[7] P. Polygerinos, N. Correll, S. A. Morin, B. Mosadegh, C. D. Onal, K. Petersen, M. Cianchetti, M. T. Tolley, R. F. Shepherd, *Adv. Eng. Mater.* **2017**, *19*, 1700016.
[8] A. De Greef, P. Lambert, A. Delchambre, *Precis. Eng.* **2009**, *33*, 311.
[9] R. V. Martinez, J. L. Branch, C. R. Fish, L. Jin, R. F. Shepherd, R. M. D. Nunes, Z. Suo, G. M. Whitesides, *Adv. Mater.* **2012**, *25*, 205.
[10] A. D. Marchese, R. K. Katzschmann, D. Rus, in *2014 IEEE/RSJ International Conf. on Intelligent Robots and Systems*, IEEE, Piscataway, NJ **2014**, pp. 554–560.
[11] H. Lipson, *Soft Rob.* **2014**, *1*, 21.
[12] M. Wehner, M. T. Tolley, Y. Mengüç, Y.-L. Park, A. Mozeika, Y. Ding, C. Onal, R. F. Shepherd, G. M. Whitesides, R. J. Wood, *Soft Rob.* **2014**, *1*, 263.
[13] M. Wehner, R. L. Truby, D. J. Fitzgerald, B. Mosadegh, G. M. Whitesides, J. A. Lewis, R. J. Wood, *Nature* **2016**, *536*, 451.
[14] W. McMahan, V. Chitrakaran, M. Csencsits, D. Dawson, I. Walker, B. Jones, M. Pritts, D. Dienno, M. Grissom, C. Rahn, in *Proc. 2006 IEEE Int. Conf. Robotics and Automation, 2006. ICRA 2006*, IEEE, Piscataway, NJ **2006**, pp. 2336–2341.
[15] Festo, *BionicSoftArm* **2019**, https://www.festo.com/de/de/e/ueber-festo/forschung-und-entwicklung/bionic-learning-network/highlights-2018-2021/bionicsoftarm-id_68209/.
[16] E. G. Hevia, C. M. McCann, M. Bell, N. Seung Patrick Hyun, C. Majidi, K. Bertoldi, R. J. Wood, *Adv. Intell. Syst.* **2022**, *4*, 2200122.
[17] N. Devaraju, M. A. Unger, *Lab Chip* **2012**, *12*, 4809.
[18] M. Rhee, M. A. Burns, *Lab Chip* **2009**, *9*, 3131.
[19] S. Hoang, K. Karydis, P. Brisk, W. H. Grover, *Plos One* **2021**, *16*, 0254524.
[20] E. C. Jensen, W. H. Grover, R. A. Mathies, *J. Microelectromech. Syst.* **2007**, *16*, 1378.
[21] A. Russomanno, R. B. Gillespie, S. O'Modhrain, M. Burns, in *2015 IEEE World Haptics Conf. (WHC)*, IEEE, Piscataway, NJ **2015**, pp. 177–182.
[22] P. Rothemund, A. Ainla, L. Belding, D. J. Preston, S. Kurihara, Z. Suo, G. M. Whitesides, *Sci. Rob.* **2018**, *3*, 16.
[23] K. Luo, P. Rothemund, G. M. Whitesides, Z. Suo, *J. Mech. Phys. Solids* **2019**, *131*, 230.
[24] W. H. Grover, A. M. Skelley, C. N. Liu, E. T. Lagally, R. A. Mathies, *Sens. Actuators, B* **2003**, *89*, 315.
[25] P. N. Duncan, S. Ahrar, E. E. Hui, *Lab Chip* **2015**, *15*, 1360.
[26] J. A. Weaver, J. Melin, D. Stark, S. R. Quake, M. A. Horowitz, *Nat. Phys.* **2010**, *6*, 218.
[27] D. Qin, Y. Xia, G. M. Whitesides, *Nat. Protoc.* **2010**, *5*, 491.
[28] L. Böswirth, S. Bschorer, *Technische Strömungslehre*, Vol. *10*, Springer **2012**.

[29] R. Darby, R. P. Chhabra, *Chemical Engineering Fluid Mechanics*, CRC Press **2016**.
[30] NovaLynx, *Elevation Correction Tables For Barometric Pressure Sensors, Technical Report*, NovaLynx Corp. **2020**.
[31] D. Drotman, S. Jadhav, D. Sharp, C. Chan, M. T. Tolley, *Sci. Rob.* **2021**, *6*, 51.
[32] W. H. Grover, R. H. C. Ivester, E. C. Jensen, R. A. Mathies, *Lab Chip* **2006**, *6*, 623.
[33] D. Bruder, R. J. Wood, *IEEE Rob. Autom. Lett.* **2022**, *7*, 542.
[34] X. Liu, W. Zuo, H. Song, T. Shang, H. Dong, L. Wang, J. Shao, S. Li, *Energies* **2022**, *15*, 8094.